

# Distributed Quantum Computing with Photons and Atomic Memories

Eun Oh, Xuanying Lai, Jianming Wen, and Shengwang Du\*

The promise of universal quantum computing requires scalable single- and inter-qubit control interactions. Currently, three of the leading candidate platforms for quantum computing are based on superconducting circuits, trapped ions, and neutral atom arrays. However, these systems have strong interaction with environmental and control noises that introduce decoherence of qubit states and gate operations. Alternatively, photons are well decoupled from the environment and have advantages of speed and timing for quantum computing. Photonic systems have already demonstrated capability for solving specific intractable problems like Boson sampling, but face challenges for practically scalable universal quantum computing solutions because it is extremely difficult for a single photon to “talk” to another deterministically. Here, a universal distributed quantum computing scheme based on photons and atomic-ensemble-based quantum memories is proposed. Taking the established photonic advantages, two-qubit nonlinear interaction is mediated by converting photonic qubits into quantum memory states and employing Rydberg blockade for the controlled gate operation. Spatial and temporal scalability of this scheme is demonstrated further. These results show photon-atom network hybrid approach can be a potential solution to universal distributed quantum computing.

gates can be rotation operators, phase shift, and controlled-NOT (CNOT) gates.<sup>[2]</sup> Currently, there are three leading candidates for quantum computer platforms: superconducting circuits,<sup>[3]</sup> trapped ions,<sup>[4]</sup> and neutral atom arrays.<sup>[5,6]</sup> Even though there are ongoing efforts to address various challenges, all these systems have strong interactions with environmental and control noises that introduce decoherence and limited lifetime for quantum computation.<sup>[7,8]</sup>

On the contrary, photons are well decoupled from the background, travel at the highest speed in the universe, and can be precisely controlled in picosecond time resolution routinely in the lab. Recently, photonic systems have demonstrated power in solving intractable problems like Boson sampling,<sup>[9]</sup> but face challenges for practically scalable universal quantum computing solutions because it is extremely difficult for a single photon to control another deterministically. Though manipulating photonic single qubits is straightforward with linear optics including wave plates, mirrors, and beam splitters,<sup>[10,11]</sup>

the path toward universal quantum computer faces a great challenge due to a lack of efficient optical nonlinearity at a single-photon level. The widely used scheme with linear optics, making use of probabilistic measurement-induced effective “nonlinearity,” is practically not efficient for large-scale implementation because it requires an enormous amount of ancilla photons and computational time.<sup>[12,13]</sup> Furthermore, there have been persistent efforts to improve the performance of linear photonic quantum computing, such as efficiency and fault tolerance,<sup>[14,15]</sup> but the nature of its nondeterminism still remains elusive.

Atomic ensemble Rydberg state mediated nonlinearity has been proposed and demonstrated for realizing photon–photon interaction gates, which requires conversion between photonic states and collective Rydberg polariton states.<sup>[16–19]</sup> However, such a quantum memory (QM) with Rydberg polaritons has very low storage-retrieval efficiency (<10% reported)<sup>[19,20]</sup> which limits its practical applications. In this article, we propose a universal quantum computing scheme based on photonic polarizations and efficient atomic-ensemble ground-state QMs. To introduce nonlinear interaction between two qubits, we convert the photonic qubit states into atomic-ensemble-based QM states and implement a two-qubit controlled-phase (CP) gate with the Rydberg blockade effect. This scheme allows for building a quantum


## 1. Introduction

Different from bits (0 and 1) in a classical digital computer, a quantum bit (i.e., qubit) is generally a superposition of two discrete states  $|0\rangle$  and  $|1\rangle$  and multiple qubits can be quantum mechanically entangled. Analogous to digital gates in a classical computer, a universal quantum computer also requires a set of basic quantum gates to operate its qubits.<sup>[1]</sup> These universal

E. Oh  
JTEC Consulting  
Decatur, GA30033, USA

X. Lai, S. Du  
Department of Physics  
The University of Texas at Dallas  
Richardson, TX 75080, USA  
E-mail: dusw@utdallas.edu

J. Wen  
Department of Physics  
Kennesaw State University  
Marietta, GA 30060, USA

 The ORCID identification number(s) for the author(s) of this article can be found under <https://doi.org/10.1002/qute.202300007>

DOI: 10.1002/qute.202300007

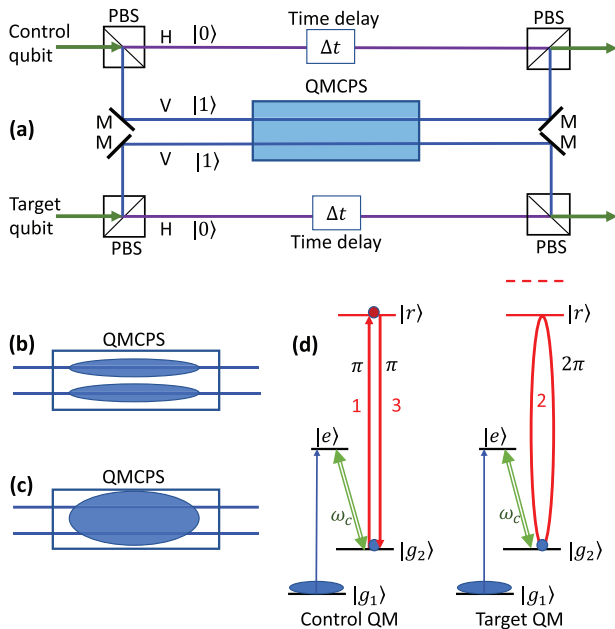


**Figure 1.** CP gate implementation scheme 1. a) The CP gate setup with polarization optics and quantum memory controlled phase shift (QMCPs) with two unoverlapping photon modes. PBS, polarizing beam splitter; M, mirror. b) QMCPs implementation with two atomic ensembles. c) QMCPs implementation with one atomic ensemble. d) The atomic energy level diagram for QM and Rydberg blockade.

computer with spatially distributed components or networking multiple remotely distributed local quantum computers.

The article is organized as follows. In Section 2, we describe two schemes for CP gate implementation. In Section 3, we describe how to implement the CNOT gate and analyze its performance as a function of QM efficiency. In Section 4, we generate  $N$ -photon Greenberger–Horne–Zeilinger (GHZ) state with CNOT gates and linear optics to show the scalability. In Section 5, we propose the QM implementation with an atomic ensemble inside a bad cavity. In Section 6, we discuss distributed quantum computing. Finally, we conclude in Section 7.

## 2. CP Gate

We present two different schemes of two-qubit CP gate with photonic qubits and atom-ensemble QM Rydberg blockade. In the first scheme, the control and target photon-atom QM modes are spatially separated and their Rydberg excitations are applied sequentially. In the second scheme, the two modes overlap spatially and require only a single Rydberg excitation pulse.

### 2.1. CP Gate Scheme 1

**Figure 1** depicts our first scheme of the photon-atom QM-mediated CP gate realization. The geometry is similar to the recently proposed implementation of atomic ensembles with non-blockade induced phase shift,<sup>[21]</sup> but we here make use of the Rydberg blockade effect which is less sensitive to the Rydberg state dephasing. As shown in **Figure 1a**, we encode the single

photon computational basis onto the two orthogonal polarizations:  $|0\rangle = |H\rangle$  (horizontal) and  $|1\rangle = |V\rangle$  (vertical). After passing through two polarizing beam splitters (PBSs), the polarizations of the control and target photons are spatially separated into four paths. The two V-polarized photon modes are injected into a QM controlled phase shift (QMCPs) unit. The QMCPs comprises two closely placed atomic ensembles with each for one photon mode as shown in **Figure 1b**, or one big atomic ensemble with two unoverlapping photon modes as shown in **Figure 1c**. After the QMCPs operation (explained later in detail), the stored photons are read out and combined with their H modes after another two PBSs. The time delays  $\Delta t$  in the two H polarization paths are used to compensate for the QMCPs operation time. When the input photon state is  $|00\rangle$ , where the first is the control qubit and the second is the target qubit, both photons pass through the two H spatial paths without any interaction and the output is still  $|00\rangle$ . When the input states are  $|01\rangle$ ,  $|10\rangle$ , and  $|11\rangle$ , the QMCPs operation is illustrated in **Figure 1d**. A QM<sup>[22,23]</sup> with electromagnetically induced transparency (EIT)<sup>[24,25]</sup> usually involves three atomic states: two long-lived hyperfine ground states  $|g_1\rangle$  and  $|g_2\rangle$  and one excited state  $|e\rangle$ . A Rydberg state  $|r\rangle$  with a large principle quantum number is used for the Rydberg blockade.<sup>[26]</sup> The qubit photons are on resonance at the transition  $|g_1\rangle \leftrightarrow |e\rangle$ . When the QM is idle, all the atoms are prepared in the state  $|g_1\rangle$  with the presence of control ( $\omega_c$ ) laser beam on resonance to the transition  $|g_2\rangle \leftrightarrow |e\rangle$ . As a V-polarized qubit photon wave packet enters the QM, we switch off the control laser and convert the photonic state into the following entangled QM state:<sup>[25]</sup>

$$|QM\rangle = \frac{1}{\sqrt{N_a}} [e^{i\phi_1} |g_2 g_1 g_1 \cdots g_1 g_1\rangle + e^{i\phi_2} |g_1 g_2 g_1 \cdots g_1 g_1\rangle + \cdots + e^{i\phi_{N_a}} |g_1 g_1 \cdots g_1 g_2\rangle] \quad (1)$$

where  $N_a$  is the number of atoms.  $\phi_j = \vec{k} \cdot \vec{r}_j$ , with  $\vec{k}$  the qubit photon wave vector, is the photon mode propagation phase at position  $\vec{r}_j$  and stores the photon momentum information. After this QM writing operation on both memories, to attain the CP gate, in a similar manner to how CP gates are implemented in neutral atom quantum computing schemes,<sup>[5,26,27]</sup> we apply the following three pulses sequentially: i) a  $\pi$  Rydberg excitation pulse on resonance at the transition  $|g_2\rangle \leftrightarrow |r\rangle$  to excite the control memory state  $|QM\rangle$  to the following collective Rydberg state

$$|QMR\rangle = \frac{1}{\sqrt{N_a}} [e^{i\phi_1} |r g_1 g_1 \cdots g_1 g_1\rangle + e^{i\phi_2} |g_1 r g_1 \cdots g_1 g_1\rangle + \cdots + e^{i\phi_{N_a}} |g_1 g_1 \cdots g_1 r\rangle]; \quad (2)$$

ii) a  $2\pi$  pulse to the resonant transition  $|g_2\rangle \leftrightarrow |r\rangle$  on the target memory; and iii) a second  $\pi$  pulse to bring the control memory back to  $|QM\rangle$ . After these three pulses, the control laser beams are switched back on to both memories and the QM state(s) is(are) then converted back to V-polarized photon(s). With the input state  $|01\rangle$ , all atoms in the control memory are in the state  $|g_1\rangle$  without Rydberg excitation such that the target memory returns to its  $|QM\rangle$  with a negative sign after the  $2\pi$  pulse. This negative sign is imprinted to the readout photon state, that is,  $|01\rangle \rightarrow -|01\rangle$ . With the input  $|10\rangle$ , there is no excitation in the target memory and the control memory state obtains a negative

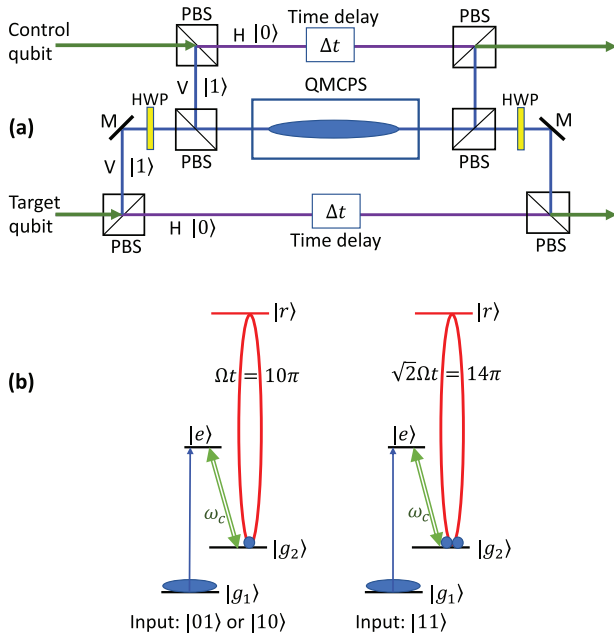


**Figure 2.** CP gate implementation scheme 2. a) The CP gate setup with polarization optics and QMCPS with only one shared atomic ensemble and two overlapping photon modes. HWP, half-wave plate. b) The atomic level diagram for QM and Rydberg blockade operations.

sign after two  $\pi$  pulses:  $|10\rangle \rightarrow -|10\rangle$ . In the case with the input  $|11\rangle$ , both memories are excited into the state  $|QM\rangle$ . After the first  $\pi$  pulse, the control memory is excited to its Rydberg state  $|QMR\rangle$ , which induces a blue energy shift for the target memory Rydberg state  $|r\rangle$  due to the dipole–dipole interaction and prevents Rydberg excitation in the target memory. This blockade effect makes the  $2\pi$  pulse on the target memory unable to complete the excitation cycle, and unable to gain a negative phase. After the second  $\pi$  pulse, the control memory returns to its  $|QM\rangle$  with a negative sign. Overall, we obtain  $|11\rangle \rightarrow -|11\rangle$  for the readout photons. In terms of the two-qubit basis  $\{|00\rangle, |01\rangle, |10\rangle, |11\rangle\}$ , the above CP gate can be described by a  $4 \times 4$  matrix

$$CP = \begin{bmatrix} 1 & 0 & 0 & 0 \\ 0 & -1 & 0 & 0 \\ 0 & 0 & -1 & 0 \\ 0 & 0 & 0 & -1 \end{bmatrix} \quad (3)$$

## 2.2. CP Gate Scheme 2

As an alternative scheme, **Figure 2** delineates our second CP gate architecture. Different from scheme 1 with two closely placed QM atomic ensembles or two unoverlapping photon modes, here we have only one ensemble capable of storing two photonic modes which overlap in space. These two modes can be two orthogonal polarizations or two momentum modes.<sup>[23]</sup> For the purpose of illustration, in this scheme, we focus on two polarization modes which have the maximum spatial overlap in the single QM atomic ensemble but keep in mind that the polarization modes can be converted into momentum modes as described in ref. [23] (see Appendix A for details). As outlined in **Figure 2a**, we transform the V polarization of the target photon into H polarization

with a half-wave plate (HWP) and combine it with the V polarization of the control photon at a PBS (and reverse at output PBS). After the photon(s) is(are) stored inside the QM, we apply one single-atom  $\Omega t = 10\pi$  Rydberg excitation pulse, with  $\Omega$  being the single-atom Rabi frequency and  $t$  the pulse length. In the case with the input  $|01\rangle$  or  $|10\rangle$ , only one atom is excited to  $|g_2\rangle$  as shown in **Figure 2b**, and the overall QM state is described by Equation(1). Hence, the  $10\pi$  Rydberg excitation pulse results in a negative sign to the QM state as well as to the retrieved photon. For the input  $|11\rangle$  case, two atoms are excited to  $|g_2\rangle$  and the QM state now becomes

$$|QM2\rangle = \sqrt{\frac{2!(N_a - 2)!}{N_a!}} [e^{i\phi_{12}} |g_2g_2g_1 \cdots g_1g_1\rangle + e^{i\phi_{13}} |g_2g_1g_2 \cdots g_1g_1\rangle + \cdots + e^{i\phi_{N_a-1, N_a}} |g_1g_1 \cdots g_1g_2g_2\rangle] \quad (4)$$

with  $\phi_{ij} = \phi_i + \phi_j$ . For brief notation, we shorthand Equation (4) as  $|QM2\rangle = |g_2g_2\rangle$ . With the same  $10\pi$  Rydberg excitation pulse applied to two atoms, the blockade mechanism leads to an oscillation between  $|g_2g_2\rangle$  and the symmetric Rydberg state  $\frac{1}{\sqrt{2}}[|rg_2\rangle + |g_2r\rangle]$  with an effective Rabi frequency  $\sqrt{2}\Omega$ .<sup>[28–31]</sup> Accordingly, the  $\Omega t = 10\pi$  Rydberg excitation pulse is effectively enhanced as  $\sqrt{2}\Omega t = 10\sqrt{2}\pi \simeq 14\pi$  by returning the QM state to  $|QM2\rangle$  with a  $\pi$ -phase shift. That is,  $|11\rangle \rightarrow -|11\rangle$  for the readout photons. In this way, we obtain the same CP gate (Equation(3)) as in scheme 1. Yet, the technical advantages between schemes 1 and 2 become apparent in the sense that the latter configuration not only improves the Rydberg blockade effect due to the perfect spatial overlap of the two photonic modes but requires only a single excitation pulse instead of three. We caution that, the difference between  $10\sqrt{2}\pi$  and  $14\pi$  induces only an average CP gate infidelity (error rate) of 0.001, which is not the limiting factor of the gate fidelity. The fidelity of a real CP gate is thus limited by other factors such as control noise and system fluctuation.

## 3. CNOT gate

The CP gate can be transformed into a standard CNOT gate with additional target single-qubit operations, as represented by the quantum circuit of **Figure 3a**. Here,  $P(-\pi/2)$  is given by

$$P(-\frac{\pi}{2}) = \begin{bmatrix} 1 & 0 & 0 & 0 \\ 0 & -i & 0 & 0 \\ 0 & 0 & 1 & 0 \\ 0 & 0 & 0 & -i \end{bmatrix} \quad (5)$$

$X(\pi/2)$  is a  $\pi/2$  rotation gate

$$X(\frac{\pi}{2}) = \frac{1}{\sqrt{2}} \begin{bmatrix} 1 & -i & 0 & 0 \\ -i & 1 & 0 & 0 \\ 0 & 0 & 1 & -i \\ 0 & 0 & -i & 1 \end{bmatrix} \quad (6)$$

For a photonic polarization qubit, an arbitrary unitary transformation can be realized with a combination of HWPs and quarter-wave plates (QWPs) by properly aligning their slow-fast axes.<sup>[10,11]</sup> The single-qubit phase gate  $P(-\pi/2)$  is realized by a QWP whose

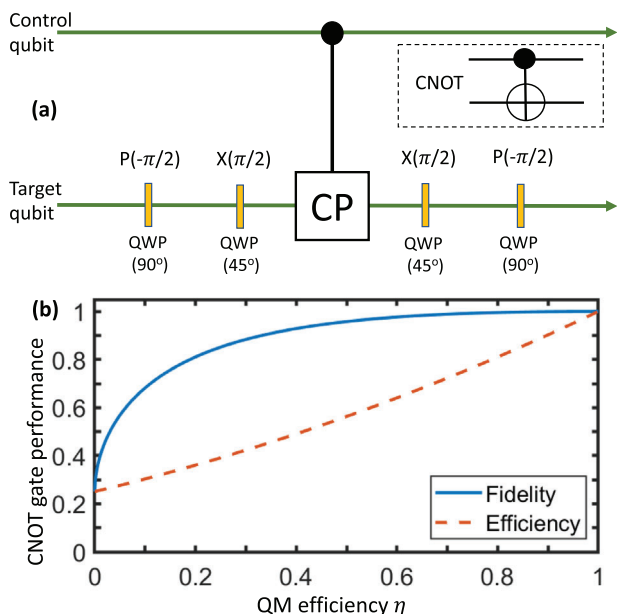


**Figure 3.** CNOT gate realization. a) Quantum circuit diagram of the CNOT gate: the CNOT gate is realized by sandwiching a CP gate in the middle of four target qubit operations. QWP, quarter-wave plate. The inset is the CNOT gate icon. b) CNOT gate fidelity and efficiency as functions of QM efficiency  $\eta$ .

fast axis is aligned along the V-polarization direction. The  $X(\pi/2)$  rotation gate is achieved by a QWP whose fast axis is aligned at  $45^\circ$  with respect to the H-polarization direction. Following the quantum circuit, we get

$$\text{CNOT} = \begin{bmatrix} 1 & 0 & 0 & 0 \\ 0 & 1 & 0 & 0 \\ 0 & 0 & 0 & 1 \\ 0 & 0 & 1 & 0 \end{bmatrix} \quad (7)$$

The QM efficiency, which is always less than unity in reality and can be modeled as photonic loss, plays an important role on the CNOT gate performance. In Figure 3b, we plot the CNOT gate fidelity and efficiency as a function of QM efficiency  $\eta$  (see Appendices B and C for details). While the fidelity remains as high as  $>0.9$  as the QM efficiency  $\eta$  drops to 0.33, the gate efficiency decreases to 0.44. This marks a significant difference between photonic and other quantum computing platforms. For the trapped-ion and atom-array systems, their gate fidelities depend strongly on the control noise as it reduces a pure qubit state into a mixed one. In our photon-atom hybrid system, the coupling between the qubit Hilbert space and environment is only caused by the loss, and the lost photons disappear into the environment but are not detected by single-photon counters. As a result, the QM loss does not affect the fidelity much but reduces the state generation efficiency as a cost.

#### 4. GHZ State Generation

As an example of scalability application, we apply the QM-mediated CNOT gates and linear optics to generate an  $N$ -photon

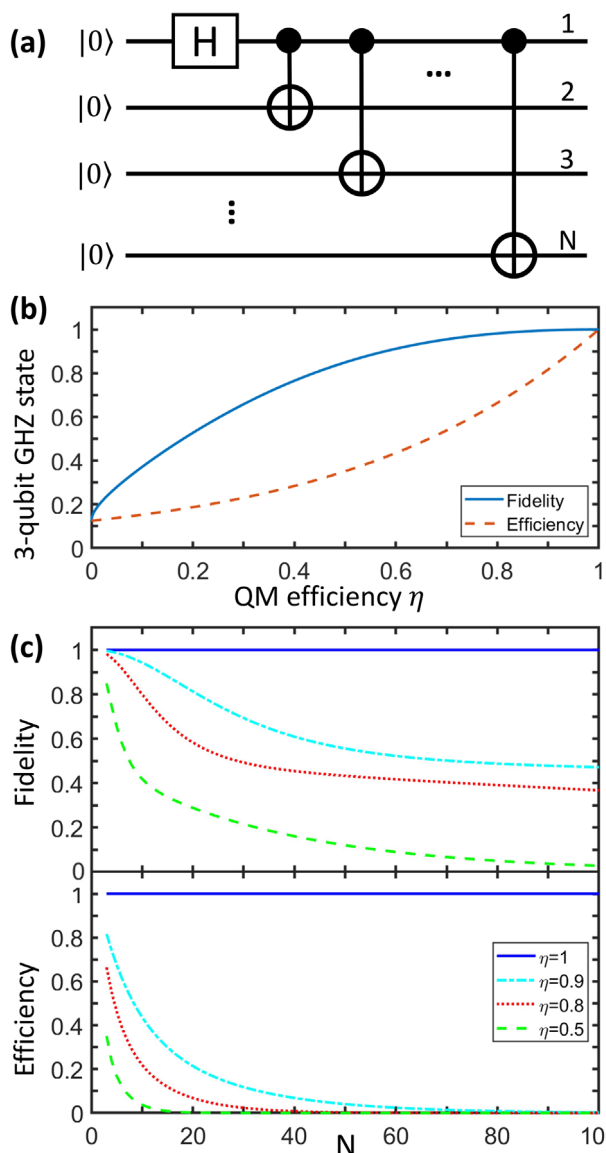


**Figure 4.** GHZ state generation. a) The quantum circuit for generating  $N$ -qubit GHZ state. b) The 3-qubit GHZ state fidelity and generation efficiency as a function of QM efficiency  $\eta$ . c)  $N$ -qubit GHZ state fidelity and generation efficiency as functions of  $N$ .

GHZ state,<sup>[32,33]</sup>  $\frac{1}{\sqrt{2}}[|000\dots\rangle + |111\dots\rangle]$ . Figure 4a is the quantum circuit with the initial (input) unentangled state prepared as  $|000\dots\rangle$ , involving  $N-1$  CNOT gates. The Hadamard (H) gate transforms the first qubit from  $|0\rangle$  to  $\frac{1}{\sqrt{2}}[|0\rangle + |1\rangle]$ , and can be implemented by an HWP with its fast axis aligned at  $22.5^\circ$  to the H-polarization axis. The fidelity and efficiency of yielding a three-photon GHZ state as a function of QM efficiency  $\eta$  is given in Figure 4b (see Appendix D for details). To have fidelity  $>0.9$ , it requires  $\eta > 0.58$  where the state generation efficiency is 0.42. To investigate the scalability, we plot the state fidelity and generation efficiency as a function of  $N$  for different  $\eta$  in Figure 4c,d, respectively. As one can see, when  $N = 100$  a fidelity  $>0.47$  is

still achievable for  $\eta = 0.9$ , but the generation efficiency reduces sharply as  $N$  increases.

## 5. Quantum Memory

As shown above, QMs are essential for the proposed schemes, providing conversion interfaces between single-photon polarization qubits and atomic states. It is extremely challenging to implement efficient QM with a single atom or ion, while an atomic ensemble has a collective enhancement under the phase-matching condition. Among various schemes including photon echo<sup>[34,35]</sup> and off-resonance Raman interaction,<sup>[36,37]</sup> so far EIT ground-state QM with laser-cooled atoms<sup>[38]</sup> has demonstrated the highest efficiency ( $\eta > 85\%$ ) for single photon polarization qubits with a fidelity of more than 99%.<sup>[23]</sup> For a single polarization channel, the memory efficiency can be as high as 90.6%.<sup>[23]</sup> Typical bandwidth of EIT quantum memory is about MHz,<sup>[39]</sup> which is determined by the atomic optical depth and control laser intensity. While in this work we are interested in polarization qubits, QMs for other degrees of freedom, such as time bins<sup>[40]</sup> and orbital angular momentum,<sup>[41]</sup> have been demonstrated.

We cautiously highlight that matrimony of an efficient QM with photonic schemes proposed here does not exist currently and the above ensemble-based QM cannot directly work for both CP schemes. For heavy alkali atoms widely used for laser cooling and trapping, such as Rb and Cs, their Rydberg interaction distance can be  $>40 \mu\text{m}$  for a large principle quantum number ( $n \geq 200$ ),<sup>[42]</sup> which is probably the limit of practical implementation. The previously demonstrated efficient QM requires a large optical depth ( $OD > 100$ ) achieved with an atomic ensemble length of about 1.0 cm,<sup>[23,38]</sup> which certainly exceeds the Rydberg blockade distance. An atomic ensemble with a length of 40  $\mu\text{m}$  can be obtained by loading laser-cooled atoms into an optical dipole trap, but the resulting OD would be only about 0.4. A possible solution to enhance OD, while maintaining free-space-like accessibility, is to put the Rydberg-blockade-distance-limited atomic ensemble into a bad cavity with a finesse  $\mathcal{F} = 800$  (see ref. [43] for the bad-cavity configuration), which leads to an enhancement factor of  $\mathcal{F}/\pi = 255$  for the effective OD

$$OD_c = \frac{\mathcal{F}}{\pi} OD_0 \quad (8)$$

where  $OD_0$  is the free-space single-pass bare OD. The above estimation is based on the typical atomic density ( $1.2 \times 10^{17} \text{ m}^{-3}$ ) in a dark-line 2D magneto-optical trap with a temperature of 20–100  $\mu\text{K}$ .<sup>[38]</sup> If we load a colder atomic ensemble or a dilute Bose–Einstein condensate with a density of  $1.0 \times 10^{18} \text{ m}^{-3}$  [44] into the same cavity, the required Rydberg blockade distance is immediately reduced to 4  $\mu\text{m}$ , which is more accessible to the existing Rydberg ( $n \leq 100$ ) excitation techniques.<sup>[42]</sup> The QM efficiency depends on the cavity-enhanced effective OD, the atomic ground-state coherence time, and the atomic density induced loss (in high density regime). Recently, trapping hundreds of microscopic atomic ensembles in optical tweezer arrays has been demonstrated,<sup>[45]</sup> which could be used for atomic-ensemble based Rydberg qubits.<sup>[30,46]</sup> Atom chip technique<sup>[47–49]</sup> may be another solution to prepare single or array of atomic ensembles.

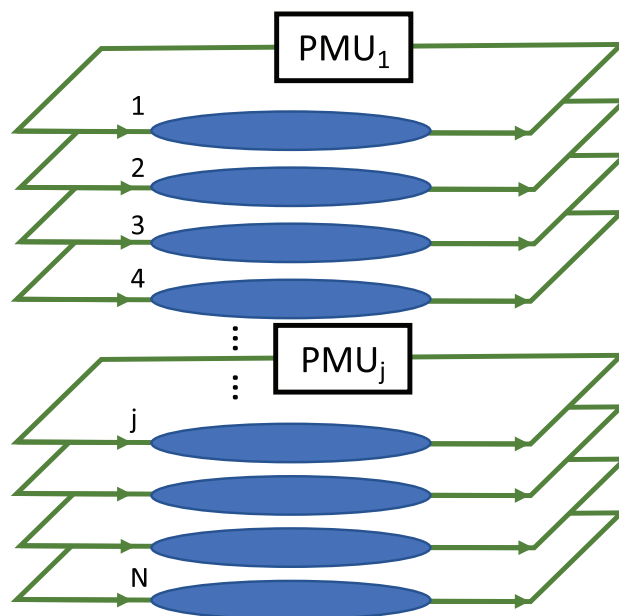


**Figure 5.** Schematics of timeline quantum computing with an array of  $N$  atomic ensemble QMs. At each QM, the readout photon is fed back to the input port after passing through a polarization manipulation unit (PMU). Each QM can store both polarization modes.

## 6. Distributed Quantum Computing

The photon-atom hybrid scheme provides a natural network interface for realizing distributed quantum computing. Here we consider two configurations of “distributed” quantum computing. In the first configuration, as described above, the quantum circuit elements are spatially distributed and connected via optical modes. Thus, our hybrid photon-atom scheme can be used to build a “distributed” quantum computer whose components are remotely located. In this configuration, a quantum computing operation or task is nonlocally distributed.

The second configuration requires networking remotely distributed local quantum computers. Our scheme can also be used to construct a timeline local quantum computer by recycling the QMs, similar to those platforms with trapped ions and neutral atoms. **Figure 5** depicts the schematics of an  $N$ -qubit quantum computer structure with a 1D (or 2D) array of  $N$  QM atomic ensembles. For each QM, its readout photon is sent back to the QM after a programmable unitary transformation—a polarization manipulation unit (PMU), which can be realized by a combination of HWPs, QWPs, and other linear optics. The nonlinear controlled gate interaction between any two-qubit memories can be mediated by the Rydberg blockade effect. However, in this configuration it is impossible to enact multiple two-qubit gates in parallel because they would interfere with each other—this is also a common challenge for the neutral atom based quantum computing community. The time-line programmable depth, or the effective coherence time, of such a quantum computer, is limited by the QM efficiency. Assuming the overall acceptable efficiency is  $\eta_t = 10\%$  and QM efficiency is  $\eta = 90\%$ , the number of programmable steps is determined by  $\ln(\eta_t)/\ln(\eta) = 22$ . To achieve more than 100 steps requires a higher QM efficiency of more

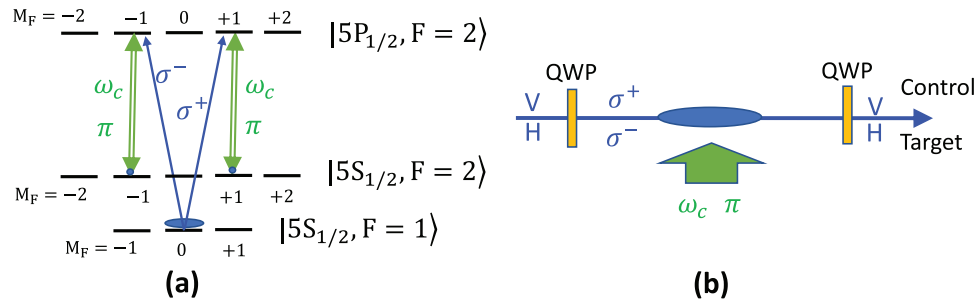


**Figure A1.** EIT for CP gate scheme 2 with two orthogonal polarizations. a) <sup>87</sup>Rb atomic energy levels. b) Optical setup.

than 98%. Different from the platforms with trapped single ions and neutral atoms whose coherence limits the computation duration, in our scheme the computation time is only limited by the photon loss, but not by the QM lifetime as it can be recycled and only requires time to complete a CP operation. As such, a local quantum computer has a naturally efficient built-in photon-atom interface, networking more than one local quantum computer with photonic links will lead to distributed quantum computing. While the current research in quantum computing<sup>[3–6]</sup> and quantum networks<sup>[51–53]</sup> are nearly isolated and there is a lack of protocol for networking distributed quantum computers, our scheme provides a natural quantum network interface between flying photons and local atomic nodes.

## 7. Conclusion

Our proposed solution incorporates the already established photonic linear manipulation and neutral atom nonlinear Rydberg interaction, encompassing building blocks not only for quantum computers but also extending its capability to quantum networks. An attractive feature of this idea is that it can be spatially and temporally distributed. We acknowledge that our initial model has unresolved physics such as QM efficiency, limited Rydberg blockade radius, and imperfect pulses which may degrade two-qubit fidelity. Nevertheless, our scheme offers scalability for both single-qubit and two-qubit controlled gates.

## Appendix A: EIT QM for CP Gate Scheme 2

Realization of the CP gate scheme 2 in Section 2.2 requires two incoming modes of the control and target qubit photons to overlap spatially inside the single QM atomic ensemble. These two modes can be two orthogonal polarizations of photons as shown in Figure 2a. We can implement such a scheme with degenerate atomic Zeeman states. Taking <sup>87</sup>Rb D<sub>1</sub> transitions as an example, we illustrate the dual EIT channels in **Figure A1a** with the Zeeman states of hyperfine energy levels  $|5S_{1/2}, F = 1\rangle$ ,  $|5S_{1/2}, F = 2\rangle$ , and  $|5P_{1/2}, F = 2\rangle$ . The atomic ensemble is prepared in the ground state  $|5S_{1/2}, F = 1, M_F = 0\rangle$  by optical pumping. The control beam ( $\omega_c$ ) with linear  $\pi$  polarization resonantly dresses the two levels  $|5S_{1/2}, F = 2\rangle$  and  $|5P_{1/2}, F = 2\rangle$  and captures the two EIT transition channels. The control qubit photon with circular polarization  $\sigma^+$  follows the EIT transition  $M_F = 0 \leftrightarrow +1 \leftrightarrow +1$ , and the target qubit photon with circular polarization  $\sigma^-$  follows the EIT transition  $M_F = 0 \leftrightarrow -1 \leftrightarrow -1$ . As these two EIT transitions are degenerate, a single Rydberg excitation pulse with proper polarization works for both control and target photonic polarization modes. Figure A1b shows the optical setup where a QWP is used to convert the two linear polarizations to two circular polarizations, and a

second QWP converts the circular polarizations back to linear polarizations.

Another approach is to take two momentum modes for the spatially overlapped control and target qubit photons. For example, as shown in **Figure A2a**, both qubit photons are  $\sigma^+$  circularly polarized and on resonance to transition  $|g_1\rangle \leftrightarrow |e\rangle$ . The control laser beam is on resonance to transition  $|g_2\rangle \leftrightarrow |e\rangle$ . Figure A2b shows one solution of the EIT optical setup with spatially overlapped control and target qubit modes sheared with a small angle.<sup>[23]</sup> Alternatively, these two momentum modes can propagate oppositely so that they can overlap maximally in space, as shown in Figure A2c, where two QWPs are used to convert linear polarizations into circular polarizations, and two PBSs are used to separate the two polarizations. During the operation of QM, the photonic momentum information is stored in the spatially varying phase of the atomic spin wave as shown in Equation (1). We have previously demonstrated that a QM efficiency of >85% is achievable for single-photon polarization qubits encoded in dual momentum modes.<sup>[23]</sup>

## Appendix B: Fidelity and Efficiency

Here we provide our theoretical models for computing the state and gate efficiency and fidelity in presence of the QM loss. Our results clearly display a significant difference between the photonic and other quantum computing platforms on performance. Specifically, for the superconducting, trapped ion, and atom-array systems, their gate fidelities depend strongly on the decoherence as it brings a pure qubit state into a mixed state. In contrast, in the photon-atom hybrid system, the coupling between the qubit Hilbert space and the environment appears only when photon loss occurs in QM. However, these lost photons vanish into the environment and fail to be detected by single-photon counters. As a result, the QM loss has little impact on the fidelity of interest, but it does reduce the state generation efficiency greatly as a cost.

As shown in the schematic in **Figures B1** and **B2**, we model the QM loss via a beam-splitter (BS) model by artificially adding two ancilla output channels, a and b, to expand the Hilbert space of the output states, rather than resorting to the mixed states basing on the same computational space as those in other platforms. In this model, except for the QM loss, we omit any other errors because those errors can be controlled quite well by the state-of-the-art linear optical technologies and hence pose no fundamental limit.

We denote the ideal output state without QM loss as  $|\varphi_1\rangle$ . In presence of optical loss to the environment, the output state with an enlarged Hilbert space takes the form of

$$|\varphi_2'\rangle = c_2|\varphi_2\rangle + c_{2\perp}|\varphi_{2\perp}\rangle \quad (\text{B1})$$

with  $|\varphi_2\rangle$  falling inside the computational Hilbert space and  $|\varphi_{2\perp}\rangle$  outside by addressing photon loss through channels a and b (see **Figures B1** and **B2**). From Equation (B1), it becomes apparent that  $\langle\varphi_2|\varphi_{2\perp}\rangle = 0$ , and  $c_2$  and  $c_{2\perp}$  satisfy the normalization condition  $|c_2|^2 + |c_{2\perp}|^2 = 1$ . These two ancilla output channels, a and b, do not exist physically but are for mathematical modeling purposes only. We “post-select”<sup>[19,50]</sup> the measurable

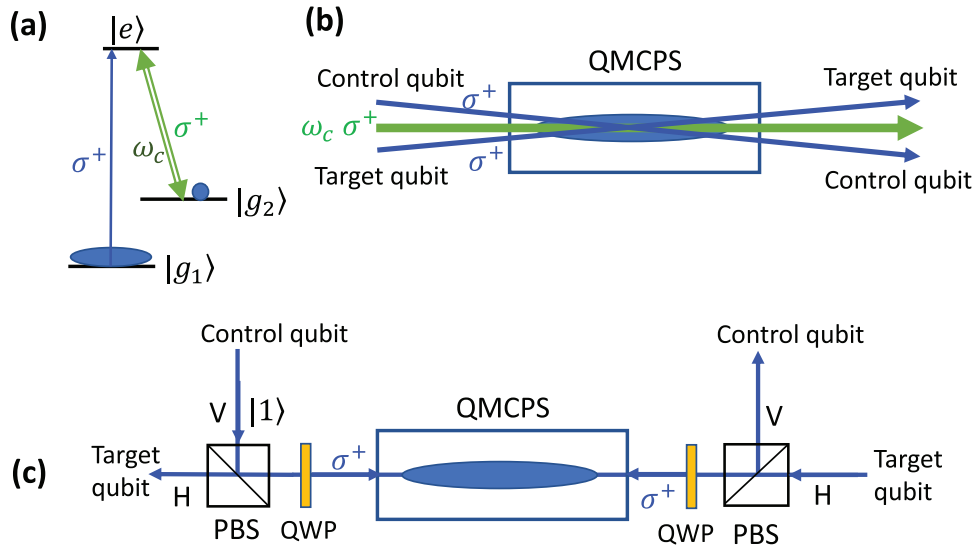


**Figure A2.** EIT for CP gate scheme 2 with the same polarization but two different momentum modes. a) EIT atomic energy level diagram. b) EIT forward optical setup with spatially overlapped control and target qubit modes sheared with a small angle. c) EIT backward optical setup with control and target qubit modes propagating in opposite directions.

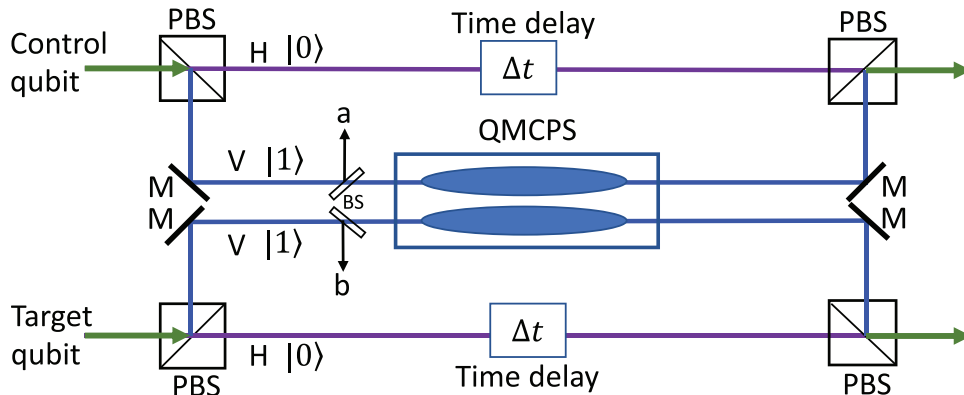


**Figure B1.** CP gate implementation scheme 1 with QM loss, which is modeled by inserting an  $\eta : 1 - \eta$  non-symmetric beam splitter (BS) in front of each QM, leading to two ancilla channels, a and b.

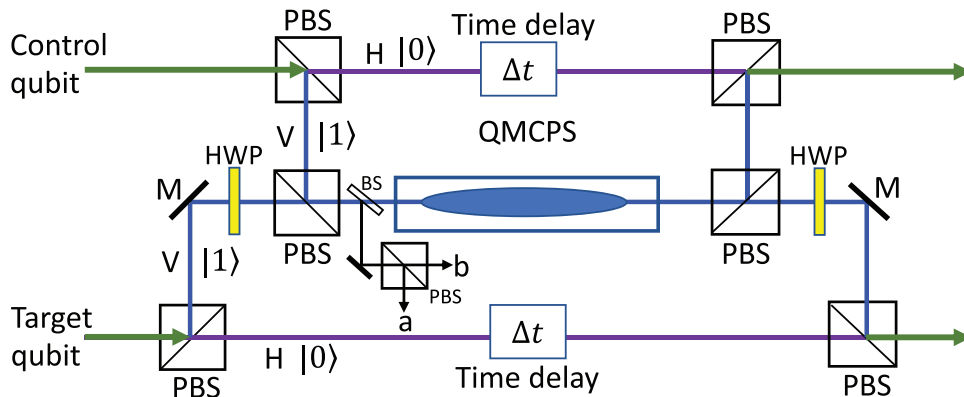


**Figure B2.** CP gate implementation scheme 2 with QM loss, which is modeled by inserting an  $\eta : 1 - \eta$  non-symmetric beam splitter (BS) in front of each QM followed by a polarizing beam splitter (PBS), leading to two ancilla channels, a and b.

**Table A1.** Expansion of basis states after BS.

Input states	States after BS
$ HH\rangle$	$ 1_H 1_H 0_a 0_b\rangle =  HH\rangle$
$ HV\rangle$	$\sqrt{\eta} 1_H 1_V 0_a 0_b\rangle + \sqrt{1-\eta} 1_H 0_V 0_a 1_b\rangle = \sqrt{\eta} HV\rangle + \sqrt{1-\eta} 1_H 0_V 0_a 1_b\rangle$
$ VH\rangle$	$\sqrt{\eta} 1_V 1_H 0_a 0_b\rangle + \sqrt{1-\eta} 0_V 1_H 1_a 0_b\rangle = \sqrt{\eta} VH\rangle + \sqrt{1-\eta} 0_V 1_H 1_a 0_b\rangle$
$ VV\rangle$	$\eta 1_V 1_V 0_a 0_b\rangle + \sqrt{\eta(1-\eta)} 1_V 0_V 0_a 1_b\rangle + \sqrt{\eta(1-\eta)} 0_V 1_V 1_a 0_b\rangle + (1-\eta) 0_V 0_V 1_a 1_b\rangle = \eta VV\rangle + \sqrt{\eta(1-\eta)} 1_V 0_V 0_a 1_b\rangle + \sqrt{\eta(1-\eta)} 0_V 1_V 1_a 0_b\rangle + (1-\eta) 0_V 0_V 1_a 1_b\rangle$

state  $|\varphi_2\rangle$  within the computational space. The state fidelity is computed as

$$F_{12} = |\langle\varphi_1|\varphi_2\rangle|^2 \quad (B2)$$

The generation efficiency  $E$  of the output state, that is, the probability of keeping photons within the computational Hilbert space, is simply

$$E = |c_2|^2 \quad (B3)$$

To evaluate the gate performance, we compute the gate fidelity by taking the average of the state fidelity over all possible inputs  $|\psi_{in}\rangle$  as

$$F_{Gate} = \overline{|\langle\varphi_1|\varphi_2\rangle|^2} = \langle|\langle\psi_{in}|\text{Gate}_1^\dagger \cdot \text{Gate}_2|\psi_{in}\rangle|^2\rangle_{\{|\psi_{in}\rangle\}} \quad (B4)$$

Here,  $\text{Gate}_1$  ( $\text{Gate}_2$ ) stands for the ideal (realistic) gate operation, and  $\dagger$  means the operation of a conjugate transpose.

### Appendix C: CNOT Gate

For CP gate scheme 1, we theoretically model its loss by inserting an  $\eta : 1 - \eta$  non-symmetric BS with transmittance  $\eta$  and reflectance  $1 - \eta$  in front of each QM, as illustrated in Figure B1. For simplicity, we assume that the input photon with the H-polarization does not experience loss; but for the V-polarized input photon, there will be the probability of  $1 - \eta$  to be reflected to two ancilla output channels a and b without being detected. Similarly, for CP gate scheme 2 as shown in Figure B2, we can model its loss by inserting an  $\eta : 1 - \eta$  non-symmetric BS in front of the common QM followed by a PBS and then perform the same analysis. Note that here the QM efficiency has already been replaced by the transmittance  $\eta$ .

After some straightforward linear algebra, we tabulate the states after the BS for different input states in **Table A1**. As shown, the QM loss of the CP gate introduces five additional bases orthogonal to the ideal computational basis  $\{|1_i 1_j 0_a 0_b\rangle\}$  ( $i, j = H, V$ ), thereby inevitably enlarging the Hilbert space. Thanks to the post-selection (i.e., single-photon detection), it allows us to reduce the Hilbert space to the computational space. Consequently, the CP gate with loss is now characterized by the following nonunitary matrix (in the computational basis),

$$\text{CP}_2 = \begin{bmatrix} 1 & 0 & 0 & 0 \\ 0 & -1 & 0 & 0 \\ 0 & 0 & -1 & 0 \\ 0 & 0 & 0 & -1 \end{bmatrix} \begin{bmatrix} 1 & 0 & 0 & 0 \\ 0 & \sqrt{\eta} & 0 & 0 \\ 0 & 0 & \sqrt{\eta} & 0 \\ 0 & 0 & 0 & \eta \end{bmatrix} \quad (C1)$$

$$= \begin{bmatrix} 1 & 0 & 0 & 0 \\ 0 & -\sqrt{\eta} & 0 & 0 \\ 0 & 0 & -\sqrt{\eta} & 0 \\ 0 & 0 & 0 & -\eta \end{bmatrix}$$

Recall the single-quit phase gate  $P(-\pi/2)$  and rotation gate  $X(\pi/2)$  given in Equation(5) in the main text. With the help of Equation (C1), one

can readily obtain the matrix of the realistic nonunitary CNOT gate as follows

$$\text{CNOT}_2 = P(-\pi/2) \cdot X(\pi/2) \cdot \text{CP}_2 \cdot X(\pi/2) \cdot P(-\pi/2)$$

$$= \begin{bmatrix} \frac{1+\sqrt{\eta}}{2} & \frac{-1+\sqrt{\eta}}{2} & 0 & 0 \\ \frac{-1+\sqrt{\eta}}{2} & \frac{1+\sqrt{\eta}}{2} & 0 & 0 \\ 0 & 0 & \frac{-\sqrt{\eta}+\eta}{2} & \frac{\sqrt{\eta}+\eta}{2} \\ 0 & 0 & \frac{\sqrt{\eta}+\eta}{2} & \frac{-\sqrt{\eta}+\eta}{2} \end{bmatrix} \quad (C2)$$

We remark that the  $\text{CP}_2$  and  $\text{CNOT}_2$  gate operations are not unitary in presence of loss ( $\eta < 1$ ). This is due to the optical losses that introduce additional dimensions to the Hilbert space. In the extended Hilbert space, where we model the losses as outputs  $a$  and  $b$  with non-symmetric beam splitters in Figures B1 and B2, the entire gate operations are still unitary, but their projections to the computational basis are nonunitary. As measuring only in the computational basis, we thus take the projected  $\text{CP}_2$  and  $\text{CNOT}_2$  gates as nonunitary operations.

We note that the ideal CNOT gate operation should read as

$$\text{CNOT}_1 = \begin{bmatrix} 1 & 0 & 0 & 0 \\ 0 & 1 & 0 & 0 \\ 0 & 0 & 0 & 1 \\ 0 & 0 & 1 & 0 \end{bmatrix} \quad (C3)$$

In presence of optical loss to the environment, for a given input state

$$|\varphi_{in}\rangle = a_{HH}|HH\rangle + a_{HV}|HV\rangle + a_{VH}|VH\rangle + a_{VV}|VV\rangle \quad (C4)$$

The output state in the enlarged Hilbert space is

$$|\varphi'_2\rangle = \text{CNOT}_2|\varphi_{in}\rangle + a_{HV}\sqrt{1-\eta}|1_H 0_V 0_a 1_b\rangle + a_{VH}\sqrt{1-\eta}|0_V 1_H 1_a 0_b\rangle$$

$$+ a_{VV}\left[\sqrt{\eta(1-\eta)}|1_V 0_V 0_a 1_b\rangle + \sqrt{\eta(1-\eta)}|0_V 1_V 1_a 0_b\rangle + (1-\eta)|0_V 0_V 1_a 1_b\rangle\right]$$

$$= c_2|\varphi_2\rangle + c_{2\perp}|\varphi_{2\perp}\rangle \quad (C5)$$

where  $|\varphi_2\rangle$  after renormalization in the computational basis is

$$|\varphi_2\rangle = \frac{\text{CNOT}_2|\varphi_{in}\rangle}{\sqrt{\langle\varphi_{in}|\text{CNOT}_2^\dagger \cdot \text{CNOT}_2|\varphi_{in}\rangle}} \quad (C6)$$

Its efficiency is

$$|c_2|^2 = \langle\varphi_{in}|\text{CNOT}_2^\dagger \cdot \text{CNOT}_2|\varphi_{in}\rangle \quad (C7)$$

In line with Equation (B4), for different input states will result in different gate efficiencies and fidelities, it becomes physically more meaningful by looking at their respective average in terms of all possible input states  $|\varphi_{in}\rangle$ . To this end, in accordance with Equations (B3) and (B4) we find the average gate efficiency and fidelity of the realistic CNOT gate to be

$$E_{\text{CNOT}} = \langle|c_2|^2\rangle_{\{|\varphi_{in}\rangle\}} \quad (C8)$$



and

$$F_{\text{CNOT}} = \langle |\langle \varphi_1 | \varphi_2 \rangle|^2 \rangle_{\{|\varphi_{\text{in}}\}} \\ = \langle \frac{|\langle \varphi_{\text{in}} | \text{CNOT}_1^\dagger \cdot \text{CNOT}_2 | \varphi_{\text{in}} \rangle|^2}{\langle \varphi_{\text{in}} | \text{CNOT}_1^\dagger \cdot \text{CNOT}_2 | \varphi_{\text{in}} \rangle} \rangle_{\{|\varphi_{\text{in}}\}} \quad (\text{C9})$$

respectively, where  $\text{CNOT}_1$  and  $\text{CNOT}_2$  are given by Equations (C3) and (C2) above.

It is worthwhile to point out that the CNOT-gate fidelity and efficiency are not zero when  $\eta = 0$ . This is because the input H-polarized photons undergo perfect propagation in our assumption. Therefore, theoretically one should get  $F_{\text{CNOT}} = E_{\text{CNOT}} = 0.25$  for  $\eta = 0$ . Interestingly, these results have been verified from our random sampling calculations as seen in Figure 3b in the main text.

## Appendix D: N-Qubit GHZ State

In this section, we present our major derivations for the generation of an  $N$ -qubit GHZ state. As illustrated in Figure 4a of the main text, since the Hardmard gate only operates on the first qubit, the input two-qubit state after the first CNOT gate becomes  $|\varphi_{\text{in}}\rangle_{12} = \frac{|00\rangle + |11\rangle}{\sqrt{2}}$  in the ideal scenario. By further extending to qubit three, according to Figure 4a in the main text, one can easily find the overall output state to be  $|\varphi_{\text{out}}\rangle_{132} = \frac{1}{\sqrt{2}}(|000\rangle + |111\rangle)$ , which is a tripartite GHZ state. If continuing to repeat the procedure, one can readily show that for  $N$  qubit inputs, the circuit is able to deliver an  $N$ -partite GHZ state  $|\text{GHZ}_1\rangle = \frac{1}{\sqrt{2}}(|0\rangle^{\otimes N} + |1\rangle^{\otimes N})$ .

For an imperfect CNOT gate (due to photon loss in the CP gate in schemes 1 and 2), however, its operation on the two components  $|00\rangle$  and  $|10\rangle$  will lead to different outputs. Specifically,

$$\text{CNOT}_2|00\rangle = \frac{1}{2}[(1 + \sqrt{\eta})|00\rangle + (-1 + \sqrt{\eta})|01\rangle] \quad (\text{D1})$$

$$\text{CNOT}_2|10\rangle = \frac{1}{2}[(-\sqrt{\eta} + \eta)|10\rangle + (\sqrt{\eta} + \eta)|11\rangle] \quad (\text{D2})$$

With these in mind, by following the quantum circuit diagram of Figure 4a in the main text, one can show that the overall state of three input qubits, after the Hardmard gate and the first CNOT gate, takes the form of

$$|\varphi_{\text{in}}\rangle_{132} = \frac{1}{2\sqrt{2}}(|00\rangle_{13} \otimes |\Phi_1\rangle_2 + |10\rangle_{13} \otimes |\Phi_2\rangle_2) \quad (\text{D3})$$

where  $|\Phi_1\rangle = (1 + \sqrt{\eta})|0\rangle + (-1 + \sqrt{\eta})|1\rangle$  and  $|\Phi_2\rangle = (-\sqrt{\eta} + \eta)|0\rangle + (\sqrt{\eta} + \eta)|1\rangle$ . As the second CNOT gate only operates on qubits 1 and 3, this will further change the state  $|\varphi_{\text{in}}\rangle_{132}$  into

$$|\varphi_{\text{out}}\rangle_{132} = \frac{1}{2^2\sqrt{2}}(|0\rangle_1 \otimes |\Phi_1\Phi_1\rangle_{32} + |1\rangle_1 \otimes |\Phi_2\Phi_2\rangle_{32}) \quad (\text{D4})$$

Extending to  $N$  qubits, by recursion, one can attain an output  $N$ -partite GHZ state with loss as following

$$|\text{GHZ}_2\rangle_N = \frac{1}{2^{N-1}\sqrt{2}}(|0\rangle_1 \otimes |\Phi_1\rangle^{\otimes(N-1)} + |1\rangle_1 \otimes |\Phi_2\rangle^{\otimes(N-1)}) \quad (\text{D5})$$

By applying Equations (B3) and (B2), the efficiency of producing such an  $N$ -qubit GHZ state, in reality, turns out to be

$$E(N) = \langle \text{GHZ}_2 | \text{GHZ}_2 \rangle_N \\ = \frac{1 + \eta^{N-1}}{2^{2N-1}} \sum_{m=0}^{N-1} P(m) \quad (\text{D6})$$

and the renormalized fidelity is

$$F_{12}(N) = \frac{|\langle \text{GHZ}_1 | \text{GHZ}_2 \rangle_N|^2}{\langle \text{GHZ}_2 | \text{GHZ}_2 \rangle_N} \\ = \frac{[(1 + \sqrt{\eta})^{N-1} + (\sqrt{\eta} + \eta)^{N-1}]^2}{2(1 + \eta^{N-1}) \sum_{m=0}^{N-1} P(m)} \quad (\text{D7})$$

where  $|\text{GHZ}_1\rangle$  is the aforementioned ideal GHZ state, and  $P(m) = C_{N-1}^m [(1 + \sqrt{\eta})^m (-1 + \sqrt{\eta})^{N-1-m}]^2$ .

When  $N = 3$ , one can use the matrix multiplication to directly obtain the output GHZ state and calculate the associated fidelity and efficiency according to the definitions given by Equations (B2) and (B3). Of course, one can also simply use Equations (D6) and (D7) to perform numerical calculations. Both ways give the same results as expected and the numerical data is shown in Figure 4b in the main text. For  $N > 3$ , we compute the fidelity and efficiency by utilizing Equations (D6) and (D7), and the results are reported in Figure 4c in the main text.

## Acknowledgements

The authors thank Mark Saffman for helpful discussions. X.L. and J.W. acknowledges support from DOE (DE-SC0022069). S.D. acknowledges support from AFOSR (FA9550-22-1-0043) and NSF (2114076 and 2228725).

## Conflict of Interest

The authors declare no conflict of interest.

## Data Availability Statement

The data that support the findings of this study are available from the corresponding author upon reasonable request.

## Keywords

quantum computing, quantum gate, quantum memory

Received: January 10, 2023

Revised: March 12, 2023

Published online: April 17, 2023

- [1] S. M. Barnett, *Quantum Information*, Oxford University Press Inc., New York **2009**.
- [2] C. P. Williams, *Explorations in Quantum Computing*, Springer, London **2011**, pp. 51–122.
- [3] J. M. Gambetta, J. M. Chow, M. Steffen, *npj Quantum Inf.* **2017**, *3*, 2.
- [4] C. D. Bruzewicz, J. Chiaverini, R. McConnell, J. M. Sage, *Appl. Phys. Rev.* **2019**, *6*, 021314.
- [5] D. S. Weiss, M. Saffman, *Phys. Today* **2017**, *70*, 44.
- [6] M. Saffman, *J. Phys. B: At., Mol. Opt. Phys.* **2016**, *49*, 202001.
- [7] W. H. Zurek, *Rev. Mod. Phys.* **2003**, *75*, 715.
- [8] M. Schlosshauer, *Rev. Mod. Phys.* **2005**, *76*, 1267.
- [9] H.-S. Zhong, H. Wang, Y.-H. Deng, M.-C. Chen, L.-C. Peng, Y.-H. Luo, J. Qin, D. Wu, X. Ding, Y. Hu, X.-Y. Yang, W.-J. Zhang, H. Li, Y.-X. Li, X. Jiang, L. Gan, G.-W. Yang, L.-X. You, Z. Wang, L. Li, N.-L. Liu, C.-Y. Lu, J.-W. Pan, *Science* **2020**, *370*, 1460.
- [10] S. Barz, *J. Phys. B: At., Mol. Opt. Phys.* **2015**, *48*, 083001.

- [11] B. E. A. Saleh, M. C. Teich, *Fundamentals of Photonics*, Wiley, New York **1991**.
- [12] E. Knill, R. Laflamme, G. J. Milburn, *Nature* **2001**, *409*, 46.
- [13] P. Kok, W. J. Munro, K. Nemoto, T. C. Ralph, J. P. Dowling, G. J. Milburn, *Rev. Mod. Phys.* **2007**, *79*, 135.
- [14] S. Bartolucci, P. Birchall, H. Bombin, H. Cable, C. Dawson, M. Gimeno-Segovia, E. Johnston, K. Kieling, N. Nickerson, M. Pant, F. Pastawski, T. Rudolph, C. Sparrow, *arXiv:2101.09310 [quant-ph]*, **2021**.
- [15] J. E. Bourassa, R. N. Alexander, M. Vasmer, A. Patil, I. Tzitrin, T. Mat-suura, D. Su, B. Q. Baragiola, S. Guha, G. Dauphinais, K. K. Sabapathy, N. C. Menicucci, I. Dhand, *Quantum* **2021**, *5*, 392.
- [16] M. D. Lukin, M. Fleischhauer, R. Cote, L. M. Duan, D. Jaksch, J. I. Cirac, P. Zoller, *Phys. Rev. Lett.* **2001**, *87*, 037901.
- [17] D. Paredes-Barato, C. S. Adams, *Phys. Rev. Lett.* **2014**, *112*, 040501.
- [18] H. Busche, P. Huillery, S. W. Ball, T. Ilieva, M. P. A. Jones, C. Adams, *Nat. Phys.* **2017**, *13*, 655.
- [19] D. Tiarks, S. Schmidt-Eberle, T. Stolz, G. Rempe, S. Dürr, *Nat. Phys.* **2019**, *15*, 124.
- [20] D. Maxwell, D. J. Szwer, D. Paredes-Barato, H. Busche, J. D. Pritchard, A. Gauguier, K. J. Weatherill, M. P. A. Jones, C. S. Adams, *Phys. Rev. Lett.* **2013**, *110*, 103001.
- [21] M. Khazali, K. Heshami, C. Simon, *Phys. Rev. A* **2015**, *91*, 030301.
- [22] S. Zhou, S. Zhang, C. Liu, J. F. Chen, J. Wen, M. M. T. Loy, G. K. L. Wong, S. Du, *Opt. Express* **2012**, *20*, 24124.
- [23] Y. Wang, J. Li, S. Zhang, K. Su, Y. Zhou, K. Liao, S. Du, H. Yan, S.-L. Zhu, *Nat. Photonics* **2019**, *13*, 346.
- [24] S. E. Harris, *Phys. Today* **1997**, *50*, 36.
- [25] M. Fleischhauer, A. Imamoglu, J. P. Marangos, *Rev. Mod. Phys.* **2005**, *77*, 633.
- [26] E. Urban, T. A. Johnson, T. Henage, L. Isenhower, D. D. Yavuz, T. G. Walker, M. Saffman, *Nat. Phys.* **2009**, *5*, 110.
- [27] L. Isenhower, E. Urban, X. L. Zhang, A. T. Gill, T. Henage, T. A. Johnson, T. G. Walker, M. Saffman, *Phys. Rev. Lett.* **2010**, *104*, 010503.
- [28] A. Gaetan, Y. Miroshnychenko, T. Wilk, A. Chotia, M. Viteau, D. Comparat, P. Pillet, A. Browaeys, P. Grangier, *Nat. Phys.* **2009**, *5*, 115.
- [29] Y. O. Dudin, L. Li, F. Bariani, A. Kuzmich, *Nat. Phys.* **2012**, *8*, 790.
- [30] Y. Mei, Y. Li, H. Nguyen, P. R. Berman, A. Kuzmich, *Phys. Rev. Lett.* **2022**, *128*, 123601.
- [31] M. Ebert, M. Kwon, T. G. Walker, M. Saffman, *Phys. Rev. Lett.* **2015**, *115*, 093601.
- [32] D. M. Greenberger, M. A. Horne, A. Zeilinger, *arXiv:0712.0921 [quant-ph]*, **2007**.
- [33] D. Bouwmeester, J.-W. Pan, M. Daniell, H. Weinfurter, A. Zeilinger, *Phys. Rev. Lett.* **1999**, *82*, 1345.
- [34] M. P. Hedges, J. J. Longdell, Y. Li, M. J. Sellars, *Nature* **2010**, *465*, 1052.
- [35] Y.-W. Cho, G. T. Campbell, J. L. Everett, J. Bernu, D. B. Higginbottom, M. T. Cao, J. Geng, N. P. Robins, P. K. Lam, B. C. Buchler, *Optica* **2016**, *3*, 100.
- [36] K. F. Reim, J. Nunn, V. O. Lorenz, B. J. Sussman, K. C. Lee, N. K. Langford, D. Jaksch, I. A. Walmsley, *Nat. Photonics* **2010**, *4*, 218.
- [37] K. F. Reim, P. Michelberger, K. C. Lee, J. Nunn, N. K. Langford, I. A. Walmsley, *Phys. Rev. Lett.* **2011**, *107*, 053603.
- [38] S. Zhang, J. F. Chen, C. Liu, S. Zhou, M. M. T. Loy, G. K. L. Wong, S. Du, *Rev. Sci. Instrum.* **2012**, *83*, 073102.
- [39] Y. Zou, Y. Jiang, Y. Mei, X. Guo, S. Du, *Phys. Rev. Lett.* **2017**, *119*, 050602.
- [40] M. Gundogan, P. M. Ledingham, K. Kutluer, M. Mazzera, H. de Riedmatten, *Phys. Rev. Lett.* **2015**, *114*, 230501.
- [41] C. Wang, Y. Yu, Y. Chen, J. Wang, X. Yang, S. Qiu, D. Wei, M. Cao, H. Gao, F. Li, *Quantum Sci. Technol.* **2021**, *6*, 045008.
- [42] M. Saffman, T. G. Walker, K. Mølmer, *Rev. Mod. Phys.* **2010**, *82*, 2313.
- [43] Y. Jiang, Y. Mei, Y. Zou, Y. Zuo, S. Du, *Rev. Sci. Instrum.* **2019**, *90*, 013105.
- [44] M. H. Anderson, J. R. Ensher, M. R. Matthews, C. E. Wieman, E. A. Cornell, *Science* **1995**, *269*, 198.
- [45] Y. Wang, S. Shevate, T. M. Wintermantel, M. Morgado, G. Lochead, S. Whitlock, *npj Quantum Inf.* **2020**, *6*, 54.
- [46] W. Xu, A. V. Venkatramani, S. H. Cantú, T. Šumarac, V. Klüsener, M. D. Lukin, V. Vuletić, *Phys. Rev. Lett.* **2021**, *127*, 050501.
- [47] S. Du, M. B. Squires, Y. Imai, L. Czaia, R. A. Saravanan, V. Bright, J. Reichel, T. W. Hänsch, D. Z. Anderson, *Phys. Rev. A* **2004**, *70*, 053606.
- [48] R. Folman, P. Kruger, J. Schmiedmayer, J. Denschlag, C. Henkel, *Adv. At., Mol., Opt. Phys.* **2002**, *48*, 263.
- [49] C. J. E. Straatsma, M. K. Ivory, J. Duggan, J. Ramirez-Serrano, D. Z. Anderson, E. A. Salim, *Opt. Lett.* **2015**, *40*, 3368.
- [50] T. Stolz, H. Hegels, M. Winter, B. Röhr, Y.-F. Hsiao, L. Husel, G. Rempe, S. Dürr, *Phys. Rev. X* **2022**, *12*, 021035.
- [51] M. Pompili, S. L. N. Hermans, S. Baier, H. K. C. Beukers, P. C. Humphreys, R. N. Schouten, R. F. L. Vermeulen, M. J. Tiggelman, L. dos Santos Martins, B. Dirkse, S. Wehner, R. Hanson, *Science* **2021**, *372*, 259.
- [52] L. J. Stephenson, D. P. Nadlinger, B. C. Nichol, S. An, P. Drmota, T. G. Ballance, K. Thirumalai, J. F. Goodwin, D. M. Lucas, C. J. Ballance, *Phys. Rev. Lett.* **2020**, *124*, 110501.
- [53] B. Jing, X.-J. Wang, Y. Yu, P.-F. Sun, Y. Jiang, S.-J. Yang, W.-H. Jiang, X.-Y. Luo, J. Zhang, X. Jiang, X.-H. Bao, J.-W. Pan, *Nat. Photonics* **2019**, *13*, 210.